Development of Models for Disk-Gap-Band Parachutes Deployed Supersonically in the Wake of a Slender Body

Clara O'Farrell
Jet Propulsion Laboratory
California Institute of Technology
Pasadena, CA 91109
818-354-8497
Clara.O'Farrell@jpl.nasa.gov

Suman Muppidi
AMA Inc.
NASA Ames Research Center
Moffett Field, CA 94035
650-604-4140
Suman.Muppidi@nasa.gov

Joseph M. Brock
AMA Inc.
NASA Ames Research Center
Moffett Field, CA 94035
650-604-6459
Joseph.M.Brock@nasa.gov

John W. Van Norman
AMA Inc.
NASA Langley Research Center
Hampton, VA 23666
757-864-7997
John.W.Vannorman@nasa.gov

Ian G. Clark
Jet Propulsion Laboratory
California Institute of Technology
Pasadena, CA 91109
818-354-0535
Ian.G.Clark@jpl.nasa.gov

Abstract— The Advanced Supersonic Parachute Inflation Research and Experiments (ASPIRE) project will investigate the supersonic deployment, inflation, and aerodynamics of Disk-Gap-Band (DGB) parachutes in the wake of a slender body. The parachutes will be full-scale versions of the DGBs used by the Mars Science Laboratory in 2012 and planned for NASA's Mars 2020 project and will be delivered to targeted deployment conditions representative of flight at Mars by sounding rockets launched out of NASA's Wallops Flight Facility. The parachutes will be tested in the wake of a slender payload whose diameter is approximately a sixth that of entry capsules used for Mars missions. Models of the deployment, inflation, and aerodynamic performance of the parachutes are necessary to design key aspects of the experiment, including: determining the expected loads and applicable margins on the parachute and payload; guiding sensor selection and placement; evaluating the vehicle trajectory for targeting, range safety, and recovery operations. In addition, knowledge of the differences in the behavior of the parachutes in the wake of slender and blunt bodies is required in order to interpret the results of the sounding rocket experiment and determine how they relate to expected performance behind blunt bodies at Mars. However, modeling the performance of a supersonic DGB in the wake of a slender body is challenging due to the scarcity of historical test data and modeling precedents. This paper describes the models of the aerodynamic performance of DGBs in supersonic slender-body wakes being developed for the ASPIRE sounding rocket test campaign. Development of these models is based on the four available flight tests of DGBs deployed in supersonic slender-body wakes as well as on data from past flight and wind-tunnel experiments of DGBs deployed in the wake of blunt bodies, on the reconstructed at-Mars DGB performance during past missions, and on computational fluid dynamics simulations. Simulations of the wakes of blunt and slender bodies in supersonic flow have been conducted in order to investigate the differences in the flowfields encountered by parachutes deployed in both wake types. The simulations have allowed the project to investigate the fundamental differences between the sounding rocket tests and the flight of a DGB during a Mars mission and to assess the limitations of the sounding rocket test architecture for evaluating flight performance at Mars.

TABLE OF CONTENTS

1. INTRODUCTION

Since the landing of the twin Viking spacecraft in 1976 [1], every United States mission to the Martian surface has used a variant of Viking's Disk-Gap-Band (DGB) parachute to decelerate from low supersonic speeds to the low subsonic speeds required for terminal descent. The DGB parachute was designed, developed, and tested during series of development campaigns undertaken by NASA in the 1960's and 1970's, which included wind tunnel testing [2], [3], [4], low altitude drop testing [5], and high-altitude supersonic parachute test programs [6], [7], [8]. Development of the DGB culminated in Viking's qualification of the 16.2-m parachute in supersonic, low-density conditions in the wake of a representative Viking entry capsule during the Balloon-Launched Decelerator Test (BLDT) series [9] and in the successful landing of Viking 1 and Viking 2 in July and September of 1976.

Following Viking's success, subsequent NASA missions to Mars successfully deployed a DGB during their descent phase: 1997's Mars Pathfinder (MPF) [10], [11], the Mars Polar Lander (MPL) two years later [12], the twin Mars Exploration Rovers (MER) in 2004 [13], the Phoenix lander in 2007 [14], and finally 2012's Mars Science Laboratory (MSL) [15]. Several modifications were made to the Viking DGB design in response to technological improvements (Kevlar suspension lines and nylon broadcloth were incorporated by MPF) and in response to mission-specific requirements. For example, the MPF project developed a DGB whose fabric band had twice the height of the Viking DGB, and the MSL project increased the trailing distance of the parachute behind the entry capsule. In addition, all missions scaled the dimensions of the DGB parachute to meet their landed mass and velocity needs: while the Phoenix project scaled the nominal diameter (D_0) of the DGB down to 11.7 m, the MSL project deployed a parachute with a nominal diameter

of 21.5 m, the largest supersonic DGB ever deployed.

While the aforementioned missions conducted subscale development tests and subsonic low-altitude qualification tests of the full scale parachutes by either drop [16] or wind tunnel testing [17], [18], none of these DGBs were qualified supersonically before their successful use on Mars. Instead, previous missions have relied on heritage data from the Viking qualification campaign to analyze the performance of their DGB designs in low density, supersonic conditions.

Recently, NASA's Low-Density Supersonic Decelerators (LDSD) project has conducted supersonic, high-altitude tests of two large parachutes for planetary exploration. The parachutes, which were 30.5 m in nominal diameter, were variants of the supersonic Ringsail parachute [19], [20]. During supersonic testing at Mach numbers above 2.0, both parachutes experienced catastrophic failure at or near full inflation, at loads well below those the parachute had been successfully tested to in subsonic low-altitude testing. In addition, scientific cameras on board the LDSD test vehicle revealed an asymmetric, dynamic, deployment and inflation process. The findings of the LDSD project have highlighted the need for supersonic, high-altitude testing of parachutes of the scale and materials necessary for future missions to Mars.

The ASPIRE Project

The Advanced Supersonic Parachute Inflation Research and Experiments (ASPIRE) project was established in 2016 to study the deployment, inflation, and performance of 21.5-m DGBs in supersonic, low-density conditions. The parachutes will be full-scale versions of the DGBs used by MSL in 2012 and planned for NASA's Mars 2020 project. They will be delivered to targeted deployment conditions representative of flight at Mars by sounding rockets launched out of NASA's Wallops Flight Facility (WFF). The first set of tests is scheduled to take place in the summer of 2017.

The concept of operations for the ASPIRE sounding rocket tests is outlined in Figure 1. The sounding rocket assembly, consisting of a Terrier first stage, a Black Brant second stage, and the 1200 kg payload section containing the experiment, will be launched from WFF. The system will be rail-launched and spin-stabilized at 4 Hz. The first and second stages will burn out at altitudes of 700 m and 16.7 km respectively, and the payload section will reach apogee at approximately 54.6 km. When the payload reaches the target dynamic pressure (q_∞) and Mach number conditions, the 21.5-m parachute will be mortar-deployed. The deployment, inflation, and supersonic and subsonic aerodynamics of the parachute will be analyzed by a suite of instruments including: a three-camera high-speed/high-resolution stereographic video system trained on the parachute, situational awareness video cameras, a set of load pins at the interface of the parachute triple-bridle and the payload, and an inertial measurement unit (IMU) onboard the payload. After decelerating to subsonic speed, the parachute and payload will descend to the ocean for recovery.

Figure 2 shows a schematic of the ASPIRE configuration after parachute deploy. The relevant dimensions of the parachute-payload system are labeled in the schematic, and their values are listed in Table 1. The parachutes will be tested in the wake of a slender payload whose diameter is approximately a sixth that of entry capsules used for Mars missions. The remaining dimensions of the ASPIRE test articles are similar to those of the MSL parachute, with the exception of the single riser which is considerably shorter in

the sounding rocket experiments [21].

Table 1. **Dimensions of the ASPIRE parachute system.**

Item	Symbol	Abs. Value	Rel. Value
Parachute reference diameter	D_0	21.5 m	-
Geometric porosity	λ_g	-	12.5%
Suspension line length	L_S	35.76 m	$\frac{L_S}{D_0} = 1.66$
Riser Length	L_R	1.0 m	
Bridle Length	L_B	1.4 m	
Forebody diameter	d	0.72 m	$\frac{D_0}{d} = 29.7$
Trailing distance	x	44 m	$\frac{x}{d} = 60.8$
Parachute projected diameter	D_P	15.5 m	$\frac{D_P}{D_0} = 0.72$

Parachute Aerodynamic Modeling

High-fidelity simulations of the test system are currently under development at the NASA Langley Research Center (LaRC) using the Program to Optimize Simulated Trajectories II (POST), and at the Jet Propulsion Laboratory (JPL) using the Dynamics Simulator for Entry, Descent, and Surface landing (DSENDS). These simulations include several models pertaining to the DGB parachute. The primary purposes of the parachute models within the POST and DSENDS simulations include:

- Determining parachute opening loads
- Evaluating the vehicle trajectory for targeting, range safety, and recovery operations
- Evaluating the conditions (Mach number, dynamic pressure) at parachute full inflation, for targeting purposes
- Determining the loads imposed by the parachute on the experiment payload
- Evaluating the accelerations (translational and rotational) imposed by the parachute on the payload
- Determining the parachute-payload dynamics, and evaluating camera coverage during parachute deployment and flight

In addition, models that account for the differences in the behavior of the parachutes in the wake of slender and blunt bodies are required in order to interpret the results of the sounding rocket experiment and determine how they relate to expected performance behind blunt bodies at Mars. However, modeling the performance of a supersonic DGB in the wake of a forebody is challenging due to the scarcity of historical test data and modeling precedents: only four supersonic flight tests of DGBs deployed in the wake of slender bodies have been successfully carried out.

This paper describes the development of models for the aerodynamic performance of DGBs in supersonic slender-body wakes for use in the ASPIRE sounding rocket test campaign. The models are based on the four available flight tests of DGBs deployed in supersonic slender-body wakes as well as on data from past flight and wind-tunnel experiments of DGBs deployed in the wake of blunt bodies, and on the reconstructed performance of DGBs during previous Mars missions. Computational fluid dynamics (CFD) simulations of the wake of blunt bodies representative of Mars entry vehicles and of the wake of slender bodies were also conducted to inform the development of the parachute models. These models will allow the project to investigate the differences in the flowfields encountered by parachutes deployed in both wake types, and to assess the fundamental differences between the sounding rocket tests and the flight of a DGB during a Mars mission.
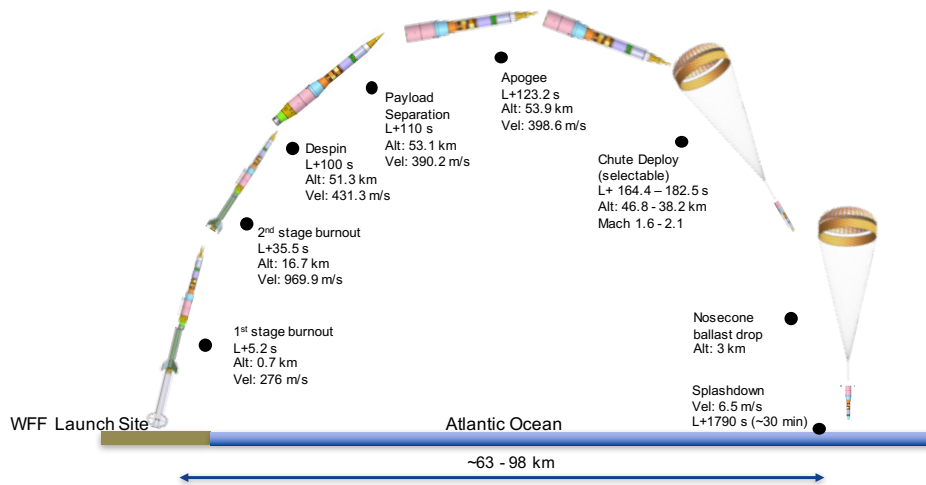
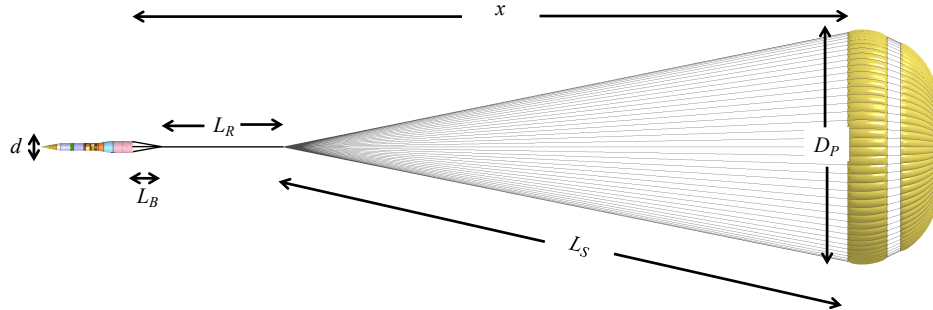**Figure 1**. ASPIRE concept of operations.

Figure 2. Schematic of the ASPIRE system.

The paper is organized as follows. A survey of past flight and wind tunnel tests of DGBs in the slender and blunt body wakes is presented in Section 2, along with an assessment of the differences in parachute performance between the two wake types. Section 3 describes the project's investigations into the supersonic wakes of slender and blunt bodies, and their effect on the dynamics of parachutes. The model for DGB inflation and aerodynamics in a slender body wake resulting from the computational study and comparison with historical results is presented in Section 4. Finally, concluding remarks and avenues for future work are presented in Section 5.

2. HISTORICAL TESTS OF SUPERSONIC PARACHUTES

Although an extensive campaign for the development of DGBs was carried out in the 1960s and 1970s, and although eight NASA missions have successfully deployed these parachutes supersonically at Mars, only four successful supersonic flight tests of DGBs deployed in the wake of slender bodies have taken place. In addition, the canopies tested in these four flights were all older designs with short suspension lines relative to the canopy nominal diameter ($L_S/D_0 = 1.0$). However, a larger class of parachutes has been flight-tested in the wake of a blunt body, and wind-tunnel-tested in the wake of both slender and blunt forebody models. Therefore, a survey of past flight and wind tunnel tests was conducted to explore the effects of flight conditions, forebody diameter, suspension line length, and trailing

distance on the inflation and aerodynamic performance of DGBs. A summary of prior low-density, supersonic tests of DGBs for which inflation data are available is presented in Table 2. Table 3 summarizes prior flight tests of DGBs in the wake of slender and blunt forebodies. Finally, a summary of prior wind tunnel tests of DGB parachutes is presented in Table 4.

The flight tests, Mars entries, and wind tunnel test campaigns listed in Tables 2 to 4 are limited to DGBs with a geometry similar to that of the MSL DGB (itself a scaled version of the Viking parachute) which will be tested during the ASPIRE campaign. Test results for the MPF, MPL, and MER DGBs, which featured a longer band than the MSL/Viking parachute, were not considered during model development. Data from wind tunnel testing of DGBs with geometrical porosities that departed significantly from Viking's 12.5% are also not included in the sections that follow. In particular, note that in NSWC TR-89-180 [22] Ludtke considered the drag performance of a large class of DGB canopy configurations. In Table 4, only those configurations that matched the ASPIRE DGB geometry most closely were included, and none of these constitute an exact match. Finally, flight tests where the canopy sustained significant damage or failed to fully inflate are not included in this study, unless otherwise noted.

It should also be noted that the parachutes listed in Tables 2 to 4 were fabricated using different materials. The canopies flown in the PEPP, SPED, SHAPE, and BLDT campaigns and the Viking flight units were manufactured using Dacron fabrics of various permeabilities, and occasionally Nomex. In

3

contrast, the MSL and Phoenix flight units were constructed using mostly PIA-C-7020D Type I nylon. Similarly, the first six tests listed in Table 4 were of Dacron construction while later tests used mostly nylon construction. Two of the wind tunnel tests listed above considered the performance of models constructed using fabrics of different permeabilities: the test at the LaRC Transonic Dynamics Tunnel (TDT) described in NESC Assessment Report 14-00932 [23], and the test at the University of Maryland (UMD) Glenn L. Martin Supersonic Pressure Tunnel (GLMWT) [22].

Supersonic DGB Inflation Tests

Table 2 presents a summary of previous flight tests featuring supersonic deployment and inflation of a DGB parachute. The Mach number and velocity of the vehicle (V_∞) at mortar fire for each inflation are listed in the table. The inflation time (t_{inf}) was defined as the time from line stretch (t_{LS}) to the first full inflation (t_{FI}) of the parachute. Inflation distance L was found by multiplying the inflation time by V_∞. A more accurate measurement of L may be found by integrating the area under the payload velocity curve, from t_{LS} to t_{FI}. However, the payload velocity curve is not available for all of the tests listed in Table 2. Where the payload velocity information was available, the difference between using the area under the velocity curve and the simplified method described above was found to be roughly 1%.

The inflations listed in Table 2 have been characterized by the non-dimensional inflation distance L/D_0. Following Greene [35], this distance can be characterized by:

$$\frac{L}{D_0} = \alpha \left(\frac{\rho_c}{\rho_\infty} \right) \quad (1)$$

where α is a canopy-specific parameter related to the parachute's volume, nominal diameter, and effective inlet area during inflation. For supersonic inflations, a normal shock is assumed to develop ahead of the canopy inlet, and the ratio of the density inside the canopy (ρ_c) to the freestream density (ρ_∞) is given by the ratio of the stagnation density behind the shock to the freestream static density [35]. Table 2 lists the calculated inflation distance and α for the supersonic inflations considered. The non-dimensional inflation distance is shown graphically as a function of deployment Mach number in Figure 3. The blue symbols represent Earth high-altitude tests of DGBs in the wake of slender bodies, while the black symbols represent DGBs also tested on Earth but in the wake of blunt bodies. The red symbols represent the available data from previous parachute deployments at Mars. The lines in the graph illustrate Greene's equation for inflation distance, for several values of α. Since the density ratio ρ_c/ρ_∞ is a function of the ratio of specific heat capacities (γ) of the inflation gas, curves representing inflation in dry air ($\gamma = 1.4$) and in carbon dioxide ($\gamma = 1.3$, representative of the Martian atmosphere) are shown in blue and red, respectively.

The data from previous supersonic deployments at Mars appear to follow Greene's formulation for $\gamma = 1.3$ quite closely, with α between 4.5 and 5.2. The BLDT results, on the other hand, appear to be bounded by values of α between 8 and 10, for $\gamma = 1.4$. The remaining two blunt-body high-Earth tests (TM-X-1499 and TM-X-2671, both represented by filled black symbols) featured parachutes with smaller L_S/D_0 ratios than the BLDT DGBs, as did all of the slender body test shown in Figure 3. In general, these canopies appeared to required longer inflation distances than the BLDT canopies tested at similar conditions, although there are exceptions such as the slender body TM-X-1623

test and the blunt body TM-X-2671 test. This may be partially related to the shorter suspension lines constraining the parachute inlet area and leading to a slower inflation. However, it should be noted that, with the exception of TM-X-2671, all tests of systems with $L_S/D_0 = 1$ also had lower canopy loading (the ratio of the payload weight to the canopy drag area , $mg/(C_D S_0)$) than the BLDT tests or Mars flights. The slower inflation observed in these tests may therefore also be a product of deviations from an ideal infinite mass case. The properties of the wake of the leading body may also play a role in determining the speed of canopy inflation, but this effect is difficult to ascertain prior to flight given the uncertainties surrounding the suspension line ratio and canopy loading.

Flight Tests of DGBs in Slender and Blunt Body Wakes

Figure 4 shows the drag coefficient as a function of Mach number for the relevant flight tests of DGB parachutes in the wake of a blunt body, both on Earth and at Mars. The high-altitude Earth tests include a single flight from the PEPP program (documented in TM-X-1499), BLDT flights AV-1, AV-2, and AV-4 (note that the canopy sustained damage during AV-1), and the at-Mars performance of the Phoenix and MSL parachutes.

In the PEPP test described in NASA TM-X-1499, the blunt forebody was jettisoned during descent, at a Mach number of 1.35. Therefore, the subsonic performance for this test corresponds to that of a parachute in the wake of a slender body. The drag coefficient of this DGB is substantially lower than that of the remaining parachutes in Figure 4. This difference is attributed to the effect of suspension line length ratio, as the DGB in question had significantly shorter suspension lines than the remaining parachutes ($L_S/D_0 = 1.02$ vs. 1.7). The model for the drag coefficient of the MSL DGB developed by that project [21] is also shown for reference in Figure 4. By design, the MSL model envelops the measured parachute C_D from all flight tests throughout the Mach number range considered, with the exception of the DGB with shorter suspension lines from TM-X-1499.

Figure 5 shows the reconstructed drag coefficient as a function of Mach number for all flight tests of DGBs in the wake of slender bodies. Only data for four high-altitude Earth tests from the PEPP, SPED, and SHAPE programs are available. All prior flight tests of DGBs in the wake of slender bodies have been of canopies with suspension line length ratios of $L_S/D_0 = 1.0$. From Figure 5, it is evident that the drag coefficients of these DGBs are significantly lower than those of the DGBs with longer suspension lines (tested in the wake of blunt bodies) shown in Figure 4. However, the drag coefficients of the DGBs shown in Figure 5 are comparable to that of the DGB with $L_S/D_0 = 1.0$ documented in TM-X-1499 and shown in Figure 4.

The MSL drag model is also shown for reference in Figure 5. The drag coefficients of the DGBs shown in Figure 5 lie close to the lower bound of the MSL drag model at all Mach numbers. Past wind tunnel studies have shown that DGBs with shorter suspension lines ($L_S/D_0 \approx 1.0$) have lower drag coefficients than equivalent parachutes with longer suspension lines, regardless of the forebody shape or trailing distance. Since the models for test on ASPIRE have $L_S/D_0 = 1.7$, the flight test data from prior tests of DGBs in the wake of slender bodies are not entirely applicable. As a result, data from previous wind tunnel tests were leveraged in order to determine how these flight test results may be applied to the ASPIRE configuration.

Table 2. **Summary of deployment conditions and calculated inflation distance L/D_0 and α for supersonic DGBs.**

Test	D_0 (m)	Mach[†]	V_∞ (m/s)[†]	t_{inf} (s)	L/D_0	α	Canopy loading (N/m^2)	Reference
PEPP	9.1	1.56	491	0.57	30.6	14.0	27	NASA TM-X-1451 [6]
PEPP*	19.7	1.59	516	0.96	25.1	11.3	14	NASA TM-X-1499 [24]
SPED	12.2	2.72	873	0.50	35.8	9.7	27	NASA TM-X-1623 [25]
SPED	12.2	1.91	616	0.69	34.9	13.0	17	NASA TM-X-1575 [7]
SHAPE	12.2	3.31	1,108	0.56	50.9	12.1	23	NASA TM-X-1924 [26]
LaRC DGB[§]	16.8	2.69	884	0.71	37.4	10.2	91	NASA TM-X-2671 [27]
BLDT AV-1[§]	16.2	2.19	705	0.66	28.8	9.4	78	NASA CR-112176 [28]
BLDT AV-2	16.2	1.08	364	0.64	14.4	9.0	71	NASA CR-112176 [29]
BLDT AV-4	16.2	2.08	698	0.59	25.3	8.6	64	NASA CR-112179 [30]
Viking 1‡	16.2	1.03	233	0.53	7.6	4.8	50	NASA CR-145148 [1]
Viking 2‡	16.2	1.06	237	0.50	7.3	4.6	113	NASA CR-145148 [1]
Phoenix‡	11.8	1.74	391	0.37	12.3	4.8	75	IEEEAC Paper 1534 [14]
MSL‡	21.4	1.75	406	0.62	11.8	4.6	71	AIAA 2013-1250 [15]

† At mortar fire.
∗ Deployed in the wake of blunt body, which was later jettisoned.
‡ At-Mars flight data from reconstruction.
§ Canopy sustained damage during test.

**Table 3**. **Summary of prior flight tests of supersonic DGBs.**

Test	D_0 (m)	Mach	λ_g (%)	D_0/d	x/d	L_S/D_0	Reference
PEPP	9.1	0.56 - 1.46	14.5	26.5	∼35	1.0	NASA TM-X-1451 [6]
PEPP*	19.7	0.4 - 1.4	12.35	4.31	4.9	1.02	NASA TM-X-1499 [24]
SPED	12.2	0.8 - 1.85	12.5	35.6	∼43	1.0	NASA TM-X-1575 [7]
SPED	12.2	1.5 - 2.6	12.5	26.5	∼35	1.0	NASA TM-X-1623 [25]
SHAPE[†]	12.2	0.1 - 0.97	12.5	35.6	∼43	1.0	NASA TN-D-6469 [8]
BLDT AV-1[§]	16.15	0.3 - 1.9	12.5	4.61	8.5	1.7	NASA CR-112176 [28]
BLDT AV-2	16.15	0.17 - 0.98	12.5	4.61	8.5	1.7	NASA CR-112177 [29]
BLDT AV-4	16.15	0.2 - 1.95	12.5	4.61	8.5	1.7	NASA CR-112179 [30]
Phoenix‡	11.8	0.6 - 1.6	12.5	4.2	8.9	1.7	IEEEAC Paper 1534 [14]
MSL‡	21.35	0.35 - 1.6	12.5	4.7	10.3	1.7	AIAA 2013-1250 [15]
ASPIRE	*21.5*	*0.2 - 1.7*	*12.5*	*29.7*	*61*	*1.7*	

∗ Deployed in the wake of blunt body, which was later jettisoned.
† Deployed in a reefed configuration. Disreef at M = 0.99.
‡ At-Mars flight data from reconstruction.
§ Canopy sustained damage during test.
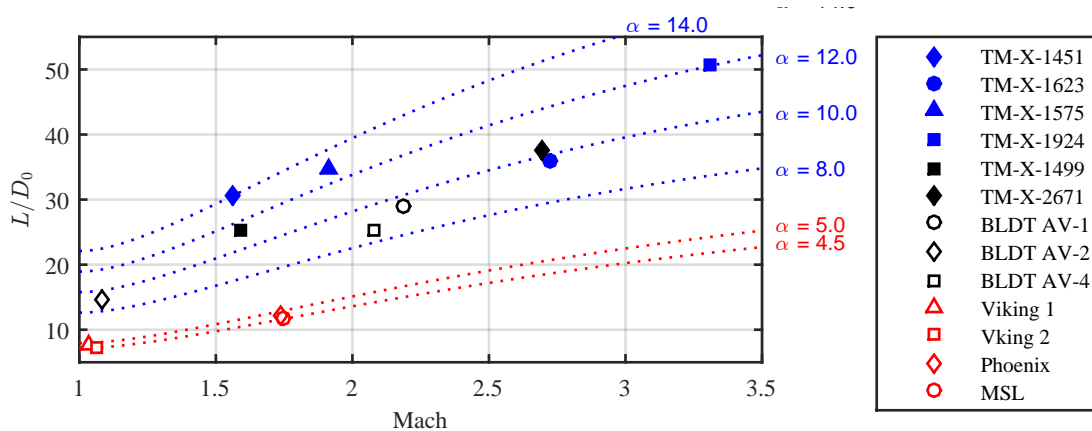
Figure 3. L/D_0 as a function of Mach number for previous supersonic DGB inflations. The blue symbols represent DGBs in the wake of slender bodies on Earth, while the black symbols represent DGBs also tested on Earth but in the wake of blunt bodies. The red symbols represent DGBs deployed at Mars. The filled symbols represent parachutes with $L_S/D_0 = 1.0$, the unfilled symbols represent parachutes with $L_S/D_0 = 1.7$.

Wind Tunnel Tests of DGBs in Slender and Blunt Body Wakes

From Table 4, it is evident that a wide class of DGB configurations have been tested in wind tunnels throughout the past four decades, in the wakes of a variety of forebody models. However, most of these tests have been limited to the subsonic, transonic, and low supersonic ranges. In fact,

5

Table 4. **Summary of prior wind tunnel tests of DGBs.**

Facility	D_0 (m)	Mach	λ_g (%)	D_0/d	x/d	L_S/D_0	Reference
AEDC 16S	1.68*	2.0 - 3.0	12.5	5.5	6.8	1.0	AEDC TR-69-245 [2]
	1.68†	1.8 - 3.0	12.5	11.7	13.6	1.0	
AEDC 16S	1.68*	2.0 - 3.0	12.5	5.5	6.8	1.0	AIAA 1970-1172 [3]
	1.68*	2.5	12.5	5.5	9.6	1.5	
AEDC 16S	1.62‡	1.8 - 2.2	12.5	4.61	6.5	1.16	AEDC TR-72-78 [31]
	1.62‡	1.8 - 2.6	12.5	4.61	8.5	1.7	
AEDC 16T	1.62‡	0.2 - 1.4	12.5	4.61	9.14	1.16	AEDC TR-72-78 [31]
	1.62‡	0.3 - 1.4	12.5	4.61	7.63	1.52	
	1.62‡	0.8 - 1.4	12.5	4.61	9.14	1.85	
	1.62‡	0.3 - 1.4	12.5	4.61	11	2.26	
	1.62§	0.2 - 1.4	12.5	4.69	6.5	1.16	
	1.62§	0.2 - 1.4	12.5	4.69	7.6	1.5	
	1.62§	0.2 - 1.4	12.5	4.69	8.5	1.7	
	1.62§	0.2 - 1.4	12.5	4.69	9.14	1.85	
	1.62§	0.2 - 1.4	12.5	4.69	11	2.26	
	1.62†	0.6 - 1.4	12.5	29.4	4.7	1.0	
	1.62†	0.6 - 1.4	12.5	29.4	4.7	1.16	
	1.62†	0.2 - 1.4	12.5	29.4	8.53	1.73	
	1.62†	0.2 - 1.4	12.5	29.4	9.14	1.85	
LaRC 4'×4'	0.254**	1.80	12.5	4.16	5.23	1.0	NASA TR-R-429 [32]
LaRC TDT	1.62‡	0.4 - 0.9	12.5	4.61	5.46	1.0	NASA CR-149377 [4]
	1.62‡	0.3 - 0.9	12.5	4.61	6.12	1.16	
	1.62‡	0.3 - 1.0	12.5	4.61	9.0	1.16	
	1.62‡	0.5 - 1.0	12.5	4.61	6.79	1.3	
	1.62†	0.4 - 0.9	12.5	NA	NA	1.16	
LaRC TDT	0.254**	0.4 - 1.2	12.5	4.2	10.5	1.0	AIAA 1973-473 [33]
	0.508**	0.4 - 1.2	12.5	4.2	10.5	1.0	
LaRC TDT††	1.43‡‡	0.1 - 0.5	12.0	4.82	10.3	1.7	NESC 14-00932 [23]
UMD GLMWT††	1.06†	0.26	13.8	13.9	19.4	1.44	NSWC TR-89-180 [22]
	1.19†	0.26	10.9	15.6	19.4	1.28	
	1.23†	0.26	11.4	16.1	19.3	1.24	
	1.29†	0.26	12.3	16.9	18.9	1.18	
GRC 10'×10'	0.81§§	2.0 - 2.5	12.5	4.76	10.6	1.7	AIAA 2008-6217 [34]
ASPIRE	*21.5*	*0.2 - 1.7*	*12.5*	*29.7*	*61*	*1.7*	

∗ Parachute tested in the wake of conical aeroshell forebody model.
† Parachute tested without a forebody model.
‡ Parachute tested in the wake of Viking entry vehicle forebody.
§ Parachute tested in the wake of Viking lander forebody.
∗∗ Parachute tested in the wake of a slender cone-cylinder forebody.
†† Tested models constructed using fabrics with two permeabilities.
‡‡ Parachute tested in the wake of MSL aeroshell forebody.
§§ Parachute tested in the wake of MSL entry vehicle forebody.

only two tests of DGBs in slender-body wakes have been conducted at Mach numbers above 1.5, and the models in question both had short suspension lines ($L_S/D_0 = 1.0$) [2], [22].

For brevity, the results from wind tunnel tests of models with suspension line length ratios other than 1.7 are not presented here. However, several trends in the historical data that aid in interpreting the results most pertinent to the ASPIRE configuration are summarized. In all tests, it was found that the C_D for DGBs tested in the wake of blunt bodies increased with L_S/D_0. As a result, the results of all wind tunnel tests of DGBs with $L_S/D_0 = 1.7$ to $L_S/D_0 = 2.26$ lay within the bounds of the MSL drag model, at all Mach numbers. However, the C_D results for DGBs with $L_S/D_0 \leq 1.3$ fell below the MSL model lower bound across the Mach number range. In addition, there appeared to be a significant deficit in C_D in the transonic region, which was more pronounced for shorter suspension line length ratios and trailing distances (x/D).

For DGBs tested in the wake of slender bodies, it was also found that the C_D of DGBs increased with L_S/D_0 at all Mach numbers. The only exception were the results from NSWC TR-89-180, which do not follow a clear trend with L_S/D_0. However, the canopies in this test also featured slight variations in other geometric properties (most notably their geometric porosity) which obscure any changes with suspension line length. For parachutes with shorter suspension line length ratios ($L_S/D_0 = 1.0$ and 1.16) tested in the wake of a slender body, there did not appear to be a significant deficit in C_D in the transonic region. However, there may be a slight drop in C_D in the transonic region for parachutes with longer suspension lines.

Comparing the C_D of DGBs with similar L_S/D_0 tested in flight and in a wind tunnel suggests that, for both slender and blunt body wakes, the parachutes tested in a wind tunnel had lower measured drag coefficients than equivalent parachutes tested in flight. The only exceptions are the subsonic results for a DGB tested in the wake of the Viking lander configu-
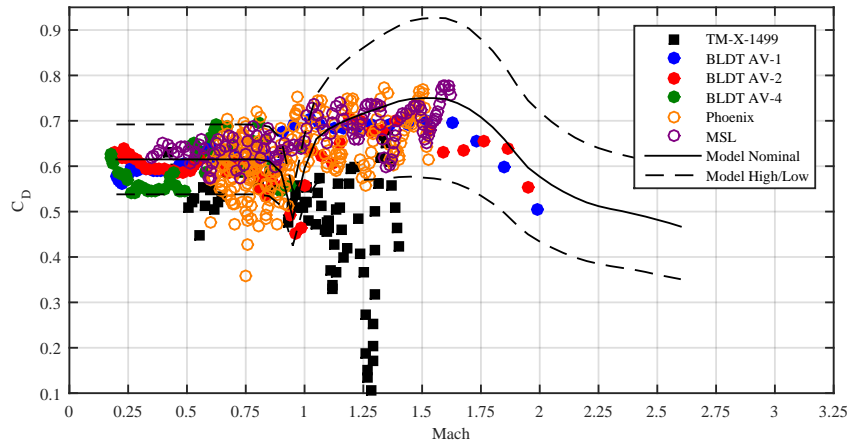
Figure 4. Normalized inflation distance as a function of Mach number for previous supersonic inflations of DGBs. The filled symbols indicate high-altitude Earth tests, and the unfilled symbols correspond to flight behavior at Mars. The square symbols denote tests of parachutes with a suspension line length ratio (L_S/D_0) of 1.0, and the circular symbols denote parachutes with $L_S/D_0 = 1.7$. The MSL drag model is shown for reference.
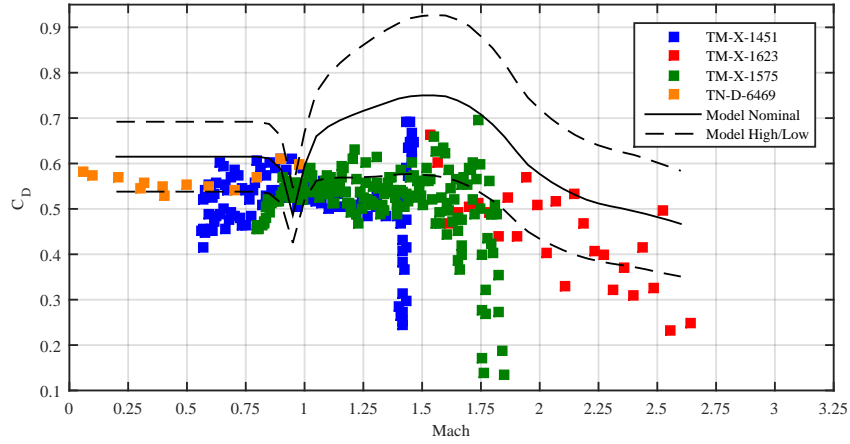
Figure 5. C_D as a function of Mach number for previous flight tests of DGBs in the wake of a slender body. The square, filled symbols indicate high-altitude Earth tests of parachutes with a suspension line length ratio (L_S/D_0) of 1.0. The MSL drag model is shown for reference.

ration from NASA TR-72-78, which agree very closely with both the flight test results and the MSL model nominal curve.

Figure 6 shows a comparison of the wind tunnel drag coefficient results for DGBs with $L_S/D_0 = 1.7$, in the wake of blunt and slender bodies. The filled symbols represent the data from tests of parachute models in the wake of a blunt body, the unfilled symbols represent the data for models tested in the wake of slender bodies, and the MSL drag model is denoted by the black lines. The MSL model envelopes both the slender and blunt body wind tunnel results, except near Mach 1. Near Mach 1, the slender body wind tunnel results show a very slight degradation in drag performance, while the blunt body results show a very large decay in C_D. Hence, the blunt body results fall slightly below the MSL model lower bound in the transonic region. For Mach numbers ranging from 0.2 to 1.4, where slender body results exist, these lie above both the blunt body wind tunnel results.

Static Aerodynamics

Historically, most wind tunnel tests of parachute systems have focused only on the drag coefficient of the parachute. Few tests aimed at characterizing the static aerodynamic coefficients of DGB parachutes have been conducted in the past. The MSL project developed a model for the static aerodynamic coefficients of the DGB based on static aerodynamics data from a wind tunnel test of various parachutes conducted by the MER project [36] in 2001. In the fall of 2014, the LDSD project and the NASA Engineering Safety Center (NESC) conducted a test of scale models of the MSL parachute in the LaRC Transonic Dynamics Tunnel (TDT) [23], [37]. The test was very similar to the test conducted by MER, and included testing of DGB models both in the wake of the MSL backshell and *without* the backshell model.

The full scale MSL DGB was constructed using mostly PIA-C-7020D Type I fabric, which has an air permeability of 80 to 120 ft^3/min/ft^2 under a differential pressure of 0.5 in of water, at sea level conditions. The DGB for the Mars 2020 project will likely use a material with similar permeability,
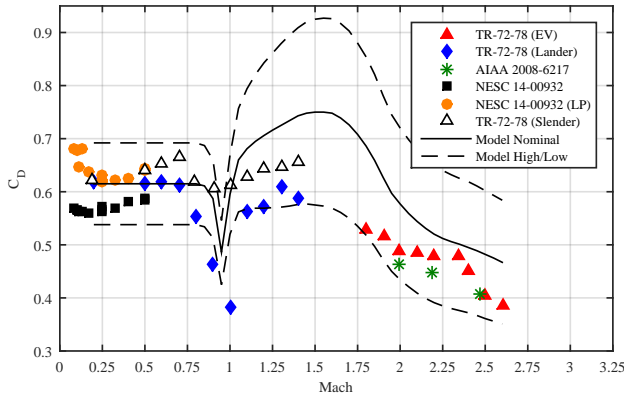
Figure 6. **Comparison of wind tunnel drag coefficient results for DGBs with a suspension line length ratio of 1.7, in the wake of blunt and slender bodies. The filled symbols represent the data from tests of parachute models in the wake of a blunt body, and the unfilled symbols represent the data for models tested in the wake of slender bodies.**

and ASPIRE test articles will be fabricated from both the MSL and Mars 2020 fabrics. However, the effective air permeability of these fabrics is dependent on the operating conditions. Therefore, the permeability of the ASPIRE canopy materials is expected to be lower at Mars and high Earth altitude conditions, than at the conditions achievable at the TDT. To capture the effect of fabric permeability, model parachutes were fabricated from both PIA-C-7020D Type I and second fabric with lower air permeability, PIA-C-44378D Type I (air permeability of 0.5-5 ft^3/min/ft^2). The effective permeability of the materials used in the ASPIRE DGBs at their intended operating conditions lies in between those of PIA-C-7020D Type I and PIA-C-44378D Type I fabrics at the wind tunnel test conditions [38].

In order to determine the sensitivity of the static aerodynamic coefficients to operating conditions, the model parachutes were tested at a set of thirteen test conditions. These conditions were selected to approximate operating conditions during terminal descent at Mars as much as possible, and spanned the range of Mach numbers from 0.1 to 0.5 and densities from 0.05 atm to 1.1 atm. The low-density test conditions were most representative of terminal descent at Mars and of the ASPIRE test conditions. However, the tests of the parachute without a forebody model were only conducted at sea level test conditions.
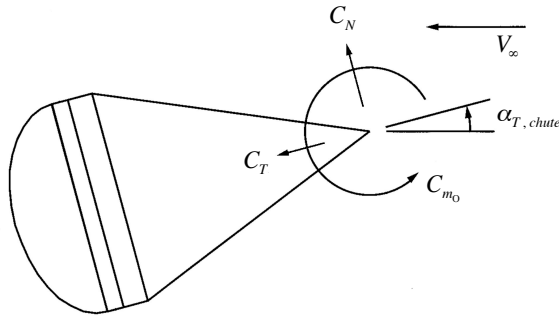
Figure 7. **Definition of the axisymmetric static aerodynamic coefficients, from Cruz *et al.***

The static aerodynamic coefficients C_T, C_N, and C_{m0} for an axisymmetric parachute are defined in Figure 7. The tangential force coefficient C_T, is aligned with the parachute symmetry axis. The normal force coefficient C_N is perpendicular to the parachute symmetry axis, and lies in the plane of the parachute total angle of attack $\alpha_{T,chute}$. The pitching moment vector defined by C_{m0} is perpendicular to the total angle of attack plane, and the reference point for the pitching moment coefficient is theoretical confluence point of the suspension lines. The pitching moment coefficient is defined using the nominal diameter D_0 as the reference length.

Figure 8 shows the curves of C_T, C_N, and C_{m0} as a function of total angle of attack for PIA-C-7020D Type I parachutes tested both in the wake of a forebody model, and without a forebody model. The red lines show the results for models tested at sea-level conditions with a forebody model. The blue lines represent a model tested at a static pressure of 0.057 atm, also with a forebody model. The green lines show the results for models tested at sea-level, without a forebody model. Figure 9 shows the same results for models constructed using PIA-C-44378D Type I. In this case, the blue lines represent a model tested at a static pressure of 0.048 atm with a forebody model.

For both PIA-C-7020D Type I and PIA-C-44378D Type I parachutes, the C_T curves for tests without a forebody lie very close to the results for parachutes tested with the MSL forebody model at the same condition, at angles of attack greater than approximately 8 deg. At small angles of attack, the parachutes tested with a forebody model show a significant C_T deficit owing to aeroshell wake effects, while the C_T curves for the no-forebody-model cases remain mostly flat. The shapes of the C_N and C_{m0} curves for parachutes constructed from both fabric types and tested without a forebody model differ from those of parachutes tested in the wake of the MSL aeroshell in similar ways. For both fabric types, parachutes tested without a forebody model show a smaller first stable trim angle of attack than parachutes tested with a forebody model. Below this stable trim angle of attack, the parachutes tested without a forebody model experience smaller disturbing pitching moments than their with-forebody counterparts. However, the no-forebody parachutes also experience smaller restoring moments past the stable trim angle of attack. In addition, the PIA-C-44378D Type I parachute tested without a forebody experiences larger disturbing pitching moments near the second unstable trim point, than the DGBs of the same fabric tested with a forebody model.

3. COMPUTATIONAL ANALYSIS OF SLENDER AND BLUNT BODY WAKES

In order to explore the observed differences in the aerodynamic performance of DGBs deployed in the slender and blunt body wakes, and to inform the development of a model for DGBs deployed in the wake of the ASPIRE sounding rockets, CFD simulations of the supersonic wakes of blunt and slender bodies are being conducted. Simulations of the wake of a blunt body representative of the MSL entry vehicle and of a slender body representative of the ASPIRE payload are being performed using US3D, a parallel unstructured implicit Navier-Stokes solver developed at the University of Minnesota and NASA Ames Research Center (ARC) [39]. Two sets of simulations are in progress. The first set considers the wake of the vehicles only, thus these simulations are being

conducted in the absence of a parachute. The simulations in the second set include a simplified, rigid DGB canopy in the wake. The chief objectives of these simulations are to contrast the mean (time-averaged) and unsteady flow features in the wakes of both leading bodies, at the approximate location of the parachute. Note that location (40 m downstream of the leading body) is about ten times the MSL diameter, and over 50 times the diameter of the slender body. In order to reliably simulate the wake dynamics over these large distances, the simulations used Detached Eddy Simulations (DES) and relied on US3D's low dissipation numerical fluxes.

All simulations are being performed at the same freestream conditions listed in Table 5. The freestream Mach number was 1.75 and the dynamic pressure was approximately 540 Pa, corresponding to an altitude of 41 km over Earth. In the future, simulations will include the MSL capsule at a freestream dynamic pressure of 540 Pa, but at a Mach number and atmospheric conditions corresponding to the altitude at parachute deploy on Mars. A subset of the simulations also include a simplified DGB canopy in the wakes of the slender body and the blunt body. The canopy is assumed to be a rigid surface of revolution with a thickness of 1.0 mm, and impervious to the flow (*i.e.* zero porosity). The leading edge of the canopy is about 40 m behind the nose of the leading body.

Table 5. **Freestream parameters for the numerical simulations**

Atmosphere	Air
Altitude	41 km over Earth
Density	0.00346 kg/m^3
Mach Number	1.75
Dynamic Pressure	538 Pa

Mean Dynamic Pressure

Figure 10 shows contours of time–averaged dynamic pressure behind the blunt body (MSL entry vehicle) and the slender body (ASPIRE sounding rocket payload) from the simulations without the simplified DGB. These contours correspond to a location 40 m downstream of the nose of the forebody. The images also show a circle whose diameter corresponds to the projected diameter of the inflated ASPIRE DGB (D_p). Note that the local dynamic pressure (q) is non-dimensionalized by the freestream dynamic pressure. The wakes are characterized by a region of low dynamic pressure towards their center, and increasing dynamic pressure away from it. As expected, the region of low dynamic pressure (the wake deficit region) is significant in the wake of the blunt body. In the slender body case, the deficit is constrained to a very small region, so that the dynamic pressure is very close to the freestream over most of the region normally occupied by the parachute. This is consistent with the observed flatness of the C_T curves shown in Figures 8 and 9.

To obtain a measure of the dynamic pressure at the location of the parachute in both cases, the mean dynamic pressure was spatially integrated over the circular region shown in Figure 10. The resulting force ($\int q dA$) was compared against the freestream equivalent ($q_\infty \pi D_p^2/4$). Although the interactions between the parachute and the wake will have a significant effect on the flow, it is expected that the dynamic pressure field at the location of the parachute will directly influence the total drag on the parachute. In the wake of the MSL forebody, the integrated dynamic pressure over the parachute projected area for a parachute aligned with the centerline of the entry

vehicle corresponded to 92% of the freestream equivalent. For the slender payload, on the other hand, the integrated dynamic pressure corresponded to over 99% of the freestream value. These results are consistent with the differences in the C_D of DGBs tested in the wake of blunt and slender bodies in wind tunnel tests (between 6% and 11% – see Section 4).

It should be noted that the present simulations consider only cases where the angle of attack of the leading vehicle is 0 deg, and where the parachute is aligned with the centerline of the leading vehicle. In reality, the attitude of the parachute and payload play a significant role in determining C_D. However, the reconstructed MSL trajectory showed that the capsule angle of attack remained below 15 deg during the parachute phase [40], and that the "pull angle" of the parachute from the capsule centerline remained below 5 deg after the initial deployment transients [15]. Future simulations and analysis will investigate the effect of the angle of attack of the leading body. In addition, the position of the parachute relative to the payload will be tracked during the ASPIRE flights using a stereographic video system. This will allow the development of a model for parachute drag based on the parachute position and wake characteristics, similar to that developed for an inflatable isotensoid ballute during the LDSD supersonic flights [41].

Temporal unsteadiness

Although the time-averaged characteristics of the blunt and slender body wakes provide an indication of the average performance of parachutes deployed in them, the time-varying, unsteady features of both flows are key to understanding transient effects in parachute behavior, peak forces, and inflation. The current simulations are being used to characterize the unsteadiness in the wakes of the blunt body and the slender body. Figure 11 shows the temporal variation of the (non-dimensional) dynamic pressure at selected points in the wake. All measurement points were located at the same axial distance (40 m downstream of the nose of the leading body) shown in Figure 10, at different radial locations. The radial measurement locations shown in the image correspond to 0.4, 1.0 and 2.0 times the diameter of the leading body.

In both cases, the flow is highly unsteady at 0.5 D (closest to the axis), and becomes increasingly steady away from the centerline. The characteristic time scale d/V_∞ (where V_∞ is the freestream velocity) is approximately six times larger for the blunt body than for the slender body. As a result, the time history of the dynamic pressure at this location shows significantly more cycles of oscillation behind the slender body, as compared to the blunt body. For both wake types, the characteristic time scale of the oscillations in the flow is considerably faster than the predicted inflation time for the DGB parachute (approximately 0.7 sec [15]).

In addition to the differences in characteristic frequency, two other features from Figure 11 bear notice. In the first place, the peak-to-peak variation in the dynamic pressure is smaller for the slender body wake than for the blunt body wake. This suggests that while a parachute inflating in the wake of a slender body would see higher-frequency oscillations in the dynamic pressure (and hence perhaps in the parachute stresses and total loads), the amplitude of these oscillations would be smaller than for a parachute inflating behind a blunt body. Secondly, while the mean dynamic pressure near the center of the wake is lower behind a blunt body than behind a slender body, the dynamic pressure for the blunt body at times approaches (and even exceeds) 90% of the freestream.

9

Note that Figure 11 presents a small subset of the data available from these simulations. Ongoing work includes analyzing the dominant frequencies and the spectral content from these simulations, and verification against available experimental data. While the information from the wake flow simulations is instructive, the presence of the DGB canopy in the wake will significantly affect both the mean and temporal flow in the wake.

Preliminary Canopy Simulations

Figure 12 shows preliminary results from simulations of flow past identical DGB canopies behind the slender body and the blunt body at the freestream conditions listed in Table 5. Figure 12 also illustrated the geometry of the slender and blunt leading bodies used in the simulations. Visually, it appears that in the case of the blunt body the wake extends until the bow shock in front of the canopy. It appears that the shock itself is affected by the wake deficit and unsteadiness. In contrast, the canopy bow shock behind the slender body appears to not be significantly affected by the wake. This difference could be attributed to one of two factors, of a combination thereof. In the first place, the smaller diameter of the slender body results in a narrower wake which affects a smaller portion of the canopy bow shock as compared to the blunt body. Secondly, the canopy leading edge in the simulations is placed 55 slender body diameters downstream of the payload nose, and only nine blunt body diameters behind the MSL entry vehicle. This increased non-dimensional separation distance results in more entrainment and mixing in the wake of the slender body, and thus a much weaker wake at the location of the canopy (as compared to the blunt body). These simulations were used to compute the aerodynamic forces on the canopy. The drag coefficient C_D of the DGB was computed as 0.78 behind the blunt body, and 0.87 behind the slender body. The drag coefficient values are consistent with the differences in the dynamic pressure field observed in simulations of the wakes without the canopy, and with the differences in the C_D of DGBs tested in a wind tunnel (Section 4).

4. ASPIRE DGB AERODYNAMICS MODEL

Deployment and Inflation Model

In this paper, parachute *deployment* refers to the events occurring between mortar firing (at $t = t_{MF}$) and suspension line stretch (at $t = t_{LS}$), defined as the time at which the canopy starts to emerge from the deployment bag. During this period, the parachute is not explicitly modeled in flight dynamics simulations, and is assumed to exert no force on the payload. The parachute is assumed to begin exerting a force on the payload at $t = t_{LS}$, where the time to line stretch is calculated from:

$$t_{LS} = t_{MF} + \frac{L_B + L_R + L_S}{29.4 \text{ m/s}} \qquad (2)$$

Here L_B, L_R, and L_S are the bridle, riser, and suspension line lengths listed in Table 1. The average bag velocity from mortar fire to line stretch was assumed to be 29.4 m/s, as in the MSL model [15].

At suspension lines stretch, the canopy begins to inflate. Unlike in the MSL model, in the ASPIRE DGB model the period from line stretch to first full inflation was modeled using an iterative process. Using Pflanz's method [42], the force exerted by the parachute during inflation was modeled as:

$$F_P = q_\infty C_D A C_X \left(\frac{t - t_{LS}}{t_{FI} - t_{LS}} \right)^n \qquad \text{for } t_{LS} \leq t \geq t_{FI}$$
$$(3)$$

$$F_P = q_\infty C_D A \qquad \text{for } t_{FI} < t \qquad (4)$$

where C_X = 1.407 is the opening force factor, and a fourth-order inflation model was assumed ($n = 4$). It is evident from the preceding equation that the computation of the time-varying force requires knowledge of t_{FI}. In the MSL model, t_{FI} was estimated by assuming an inflation velocity (V_{inf} = 30 m/sec) :

$$t_{FI} = t_{LS} + \frac{D_0}{V_{inf}} \qquad (5)$$

In the present model, the parachute inflation time (t_{inf}) was defined as the time required for the payload to travel the distance inflation distance L, as described in Section 2. However, the time required for the payload to travel the distance L is determined by the deceleration of the payload during inflation. The payload deceleration is heavily dependent on F_P, as given by Equation 3, which requires knowledge of the inflation time. As a result, an initial estimate of the inflation time was obtained from Equation 5, and used to estimate F_P for $t_{LS} \leq t \geq t_{FI}$. Using this estimate of the parachute total force, the time required for the payload to travel the inflation distance L was determined by integration of the equations of motion for the parachute-payload system. This yielded a new estimate of the inflation time, which was used to refine the estimate of F_P. This process was repeated until convergence was achieved.

The inflation distance was calculated from Equation 1, as a function of the Mach number and density at mortar fire, assuming $\gamma = 1.4$ for dry air. Based on the past supersonic inflations of DGBs with $L_S/D_0 = 1.6$ on Earth and at Mars, the inflation distance parameter was assumed to have a nominal value of $\alpha = 7$. In Monte Carlo simulations, it was assumed to vary uniformly between $\alpha = 5$ and $\alpha = 9$.

Drag Model

An updated model for the drag coefficient of DGBs in the wake of a slender body was developed for the ASPIRE campaign. The model used the MSL drag model as a baseline, and was informed by the findings described in sections 2 and 3. Figure 13 shows the ASPIRE DGB drag model, along with the MSL model.

At subsonic speeds, the wind tunnel test results for MSL-like DGBs in the wake of a slender body were found to be slightly larger than the blunt body wind tunnel results, by between 1% and 12%. As a result, the nominal drag model and the upper bound curve of the ASPIRE model are approximately 5% greater than the MSL model in this regime. Due to the scarcity of slender-forebody data, and the uncertainty surrounding forebody wake effects, the lower bound curve of the ASPIRE model was left unchanged from the MSL model. As discussed in Section 2, the deep well in C_D around Mach 1 in the MSL model does not appear to be present in either the wind tunnel or flight data for slender body wakes. As a result, the magnitude and abruptness of the transonic drag well was decreased in the ASPIRE model.

At supersonic speeds, the slender body wind tunnel results for DGBs with $L_S/D_0 = 1.7$ were found to be larger than the blunt body results by 6% to 11% (Figure 6). These

findings are consistent with the studies of the time-averaged wake properties described in Section 3. In addition, the drag coefficients measured in wind tunnels for both blunt and slender bodies were found to be lower than the flight test results of equivalent parachutes by comparable amounts (approximately 15%), which suggests that the differences observed in wind tunnel tests may be translated to flight predictions. Based on these results, the C_D of MSL-like DGBs deployed in the wake of slender bodies was expected to be larger than that of equivalent parachutes deployed in bluff-body wakes at Mach numbers above 1.1. However, since the nominal curve in the MSL model has over-predicted the supersonic C_D in all flight tests to date, a modest increase to the nominal C_D curve of 5% was considered appropriate. The upper bound of the ASPIRE model was not modified relative to the MSL model in most of the supersonic regime, as wake studies suggest that the peak drag may be comparable for both slender and wake bodies, and the MSL curve was believed to be appropriately conservative in general. However, the upper bound of the ASPIRE model was increased between Mach 1.75 and Mach 2.25, the target range for parachute deployment on ASPIRE. Since this model is used for targeting the desired test conditions during the sounding rocket campaign, an increase in this region provides additional margin against the possibility of overloading the parachute at full inflation.

Static Aerodynamics

From examination of the data from the TDT test, an updated DGB static aerodynamics model was developed. Figure 14 shows the C_T, C_N and C_{m0} curves at Mach = 0.2 from the ASPIRE model. Three curves (nominal, Boundary 1, and Boundary 2) are provided for each of the static aerodynamic coefficients. The boundary curves define the uncertainty of the nominal values, and these uncertainty boundaries are correlated across C_T, C_N and C_{m0}. Relative to the MSL model, the C_T curves have been flattened at small angles of attack, to reflect the smaller wake deficit associated with slender forebodies seen in the CFD results as well as the results of the TDT test. The TDT results for the PIA-C-7020D Type I parachute tested without a forebody model were used to define the C_N and C_{m0} Boundary 2. The nominal C_N and C_{m0} curves follow the TDT results for the PIA-C-44378D Type I parachute tested without a forebody model, up to an angle of attack of 8 deg. Beyond 8 deg, the nominal model curve follows a shape similar to that of the Boundary 2 curve. In order to allow for parachutes having a stable trim angle of attack in excess of 15 deg, the model Boundary 1 C_N curve dips below the nominal and Boundary 2 curves for $\alpha_{T,chute} \leq 4$ and remains relatively constant until $\alpha_{T,chute} = 12$, when it rises and crosses the $C_N = 0$ axis at 16 deg.

5. CONCLUSIONS AND FUTURE WORK

Models for the aerodynamic performance of 21.5-m DGB parachutes deployed supersonically in the wake of a slender body are being developed by the ASPIRE program. These parachutes will be tested in a high-altitude sounding rocket campaign, starting in the summer of 2017. The models have been implemented into flight dynamics simulations of the ASPIRE systems, and are being used to determine the expected loads and applicable margins on the parachute and payload, guide sensor selection and placement, and evaluate the vehicle trajectory for targeting, range safety, and recovery operations. The models described herein differ from past models of supersonic DGBs (such as those used for the MSL project [15]) in that they apply to parachutes deployed in the wake of a slender payload section whose diameter is approximately one sixth of the diameter of a Martian entry vehicle. The models are therefore being developed based on the results of past flight tests, of wind tunnel tests of parachutes tested in blunt and slender body wakes, and on CFD simulations of the supersonic wakes of blunt and slender bodies.

Future work will focus on increasing the fidelity of the CFD simulations, and on leveraging the results of the modeling and simulation efforts to understand the fundamental differences between the sounding rocket experiment and EDL at Mars. In particular, future simulations will account for the effect of the angle of attack of the leading body on its wake, as well as the position of the parachute. The ASPIRE project plans to conduct a series of sounding rocket tests, allowing sufficient time for reconstruction of flight events and parachute performance between each successive flight. Therefore, the results of the early sounding rocket tests will be leveraged to improve and fine-tune the models described in this study, and to guide future CFD simulations, in preparation for later flights.
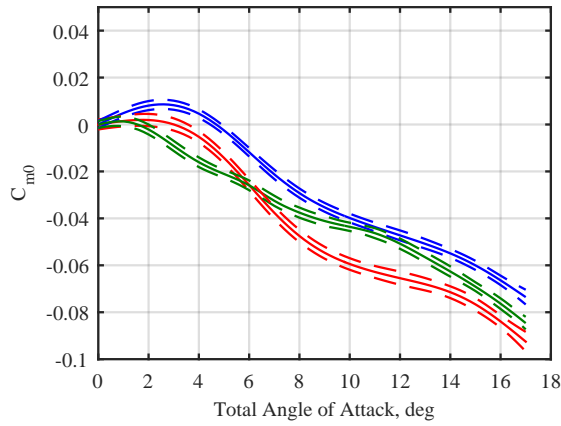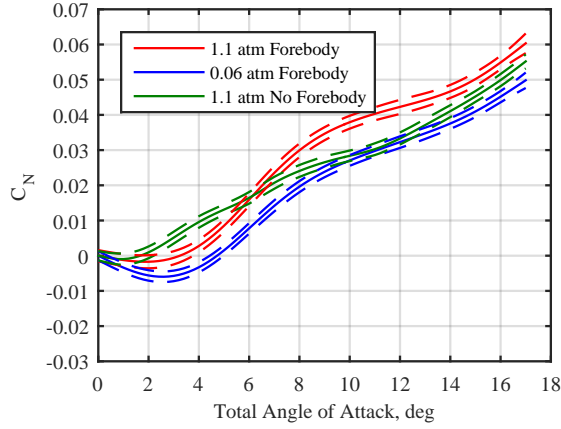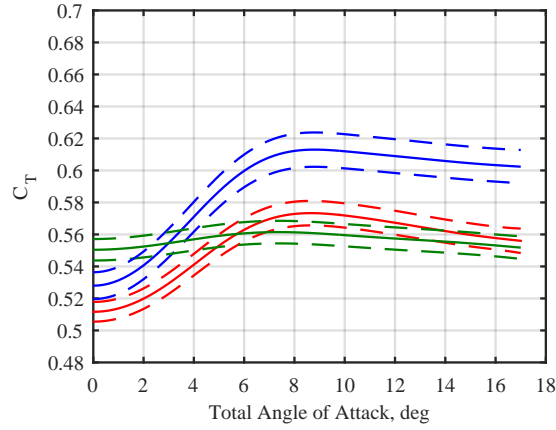
**Figure 8**. C_T, C_N and C_{m0} at **Mach = 0.2, for PIA-C-7020D Type I DGBs, tested with and without forebody models. Red lines: results at TC 3 with forebody model. Blue lines: results at TC 12 with forebody model. Green lines: results at TC 3 without forebody model. The dashed lines represent the 95% confidence interval.**
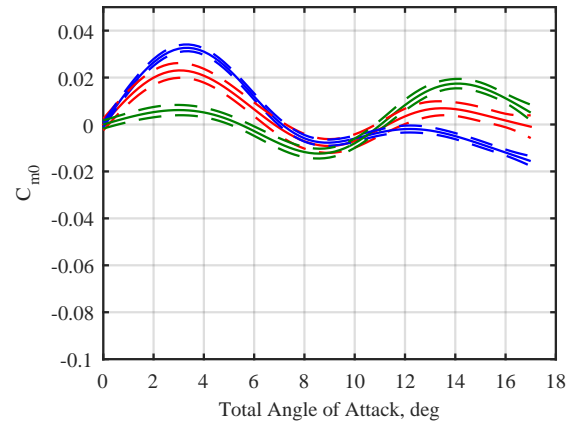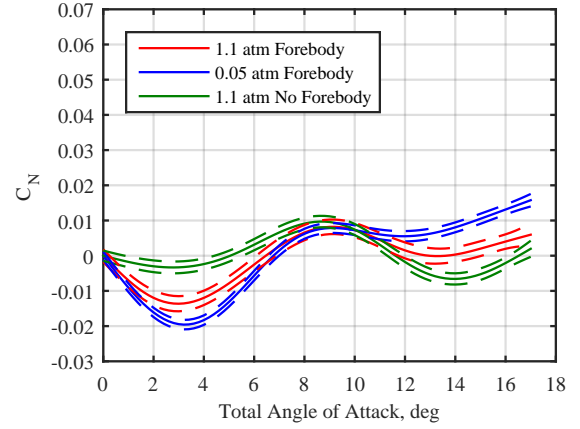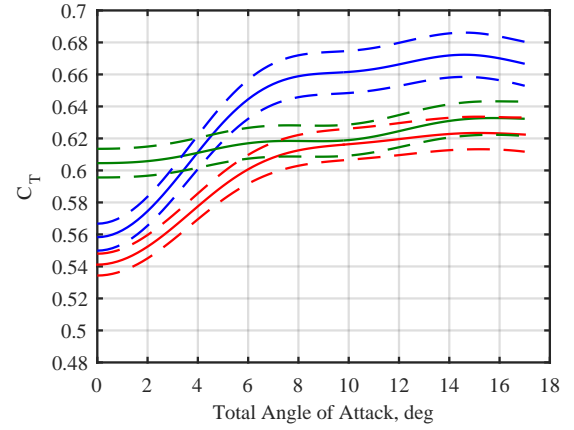
Figure 9. C_T, C_N and C_{m0} at **Mach = 0.2, for PIA-C-44378D Type I DGBs, tested with and without forebody models. Red lines: results at TC 3 with forebody model. Blue lines: results at TC 13 with forebody model. Green lines: results at TC 3 without forebody model. The dashed lines represent the 95% confidence interval.**
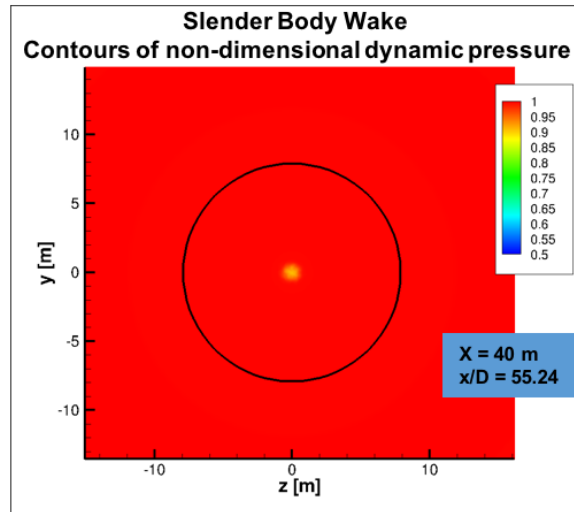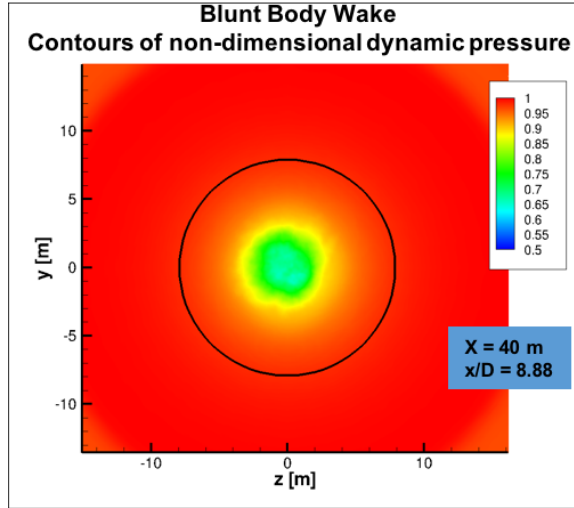
Figure 10. **Variation of mean non-dimensional dynamic pressure in the wake of the leading bodies.** The contours correspond to a location 40 m downstream of the nose of the leading vehicle, and the black circle shows the approximate extent of the inflated DGB.
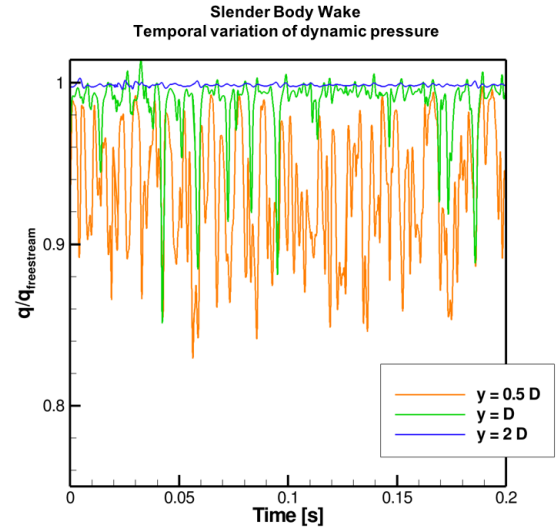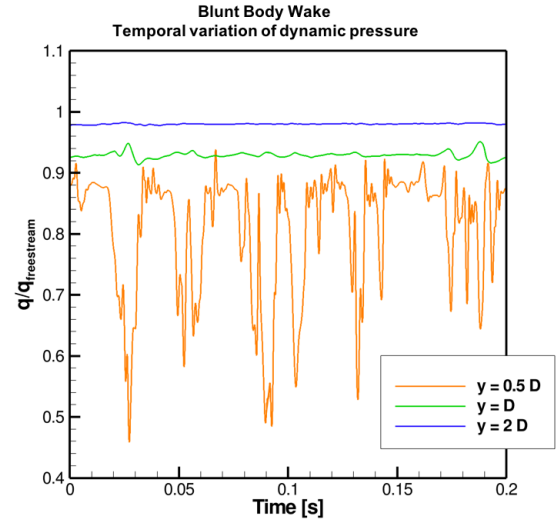

Figure 11. **Temporal variation of the non-dimensional dynamic pressure in the wakes of the blunt body and the slender body.** This variation corresponds to an axial distance of 40 m behind the nose, and at various radial distances, as function of the diameter.

13
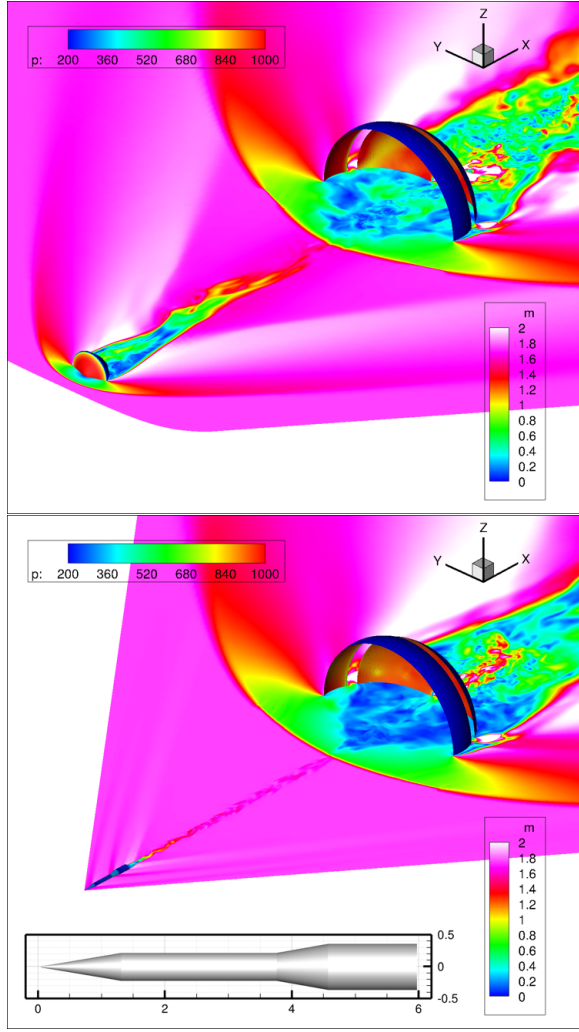
Figure 12. **Contours of fluid Mach number and surface pressure (in Pa), from simulations of a DGB canopy in the wakes of a blunt body and a slender body.** Note that most of the canopy bow shock seems unperturbed by the slender body wake.
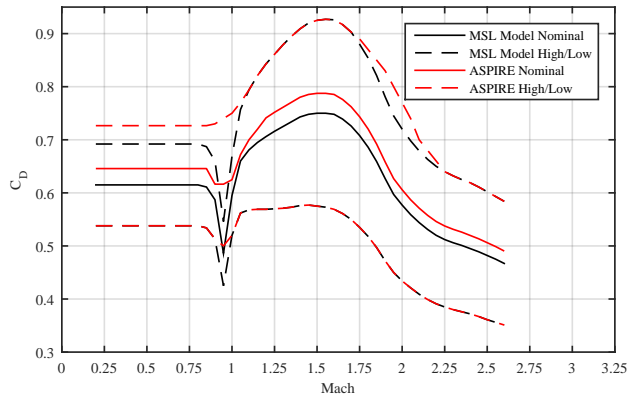
Figure 13. **ASPIRE drag model**
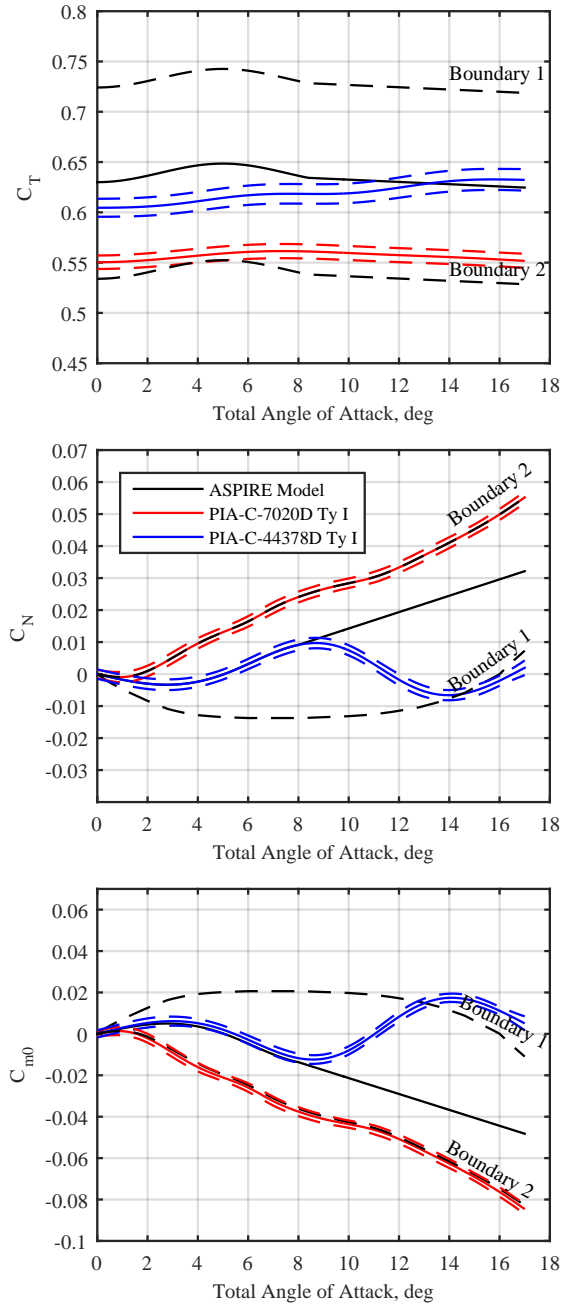
Figure 14. **ASPIRE model C_T, C_N and C_{m0} at Mach = 0.2. Black lines: nominal (solid) and upper and lower bound (dashed) curves from the SHARPIE model. Red lines: PIA-C-7020D Type I DGBs. Blue lines: PIA-C-44378D Type I GBDs. For both parachute fabrics, the dashed lines represent the 95% confidence interval.**

14

REFERENCES

[1] C. G. Cooley and J. G. Lewis, "Viking 75 Project: Viking Lander System Primary Mission Performance Report," Tech. Rep. CR-145148, Apr 1977.

[2] L. L. Galigher, "Aerodynamic Characteristics of Ballutes and Disk-Gap-Band Parachutes at Mach Numbers From 1.8 to 3.7," Tech. Rep. AEDC-TR-69-245, 1969.

[3] P. J. Bobbitt, R. J. Mayhue, G. L. Faurote, and L. L. Galigher, "Supersonic and Subsonic Wind-Tunnel Tests of Reefed and Unreefed Disk-Gap-Band Parachutes," Tech. Rep. 1970-1172, 1970.

[4] I. Jaremenko, S. Steinberg, and R. Faye-Petersen, "Scale Model Test Results of the Viking Parachute System at Mach Numbers From 0.1 Through 2.6," Tech. Rep. CR-149377, 1971.

[5] C. V. Eckstrom and H. N. Murrow, "Flight Tests of Cross, Modified Ringsail, and Disk-Gap- Band Parachutes from a Deployment Altitude of 3.05 km (10,000 ft)," Tech. Rep. TM X-2221, June 1971.

[6] C. V. Eckstrom and J. S. Preisser, " Flight Test of a 30-Foot-Nominal-Diameter Disk-Gap-Band Parachute Deployed at a Mach Number of 1.56 and a Dynamic Pressure of 11.4 Pounds Per Square Foot," Tech. Rep. TM X-1451, Aug 1967.

[7] J. S. Preisser and C. V. Eckstrom, "Flight Test of a 40-Foot-Nominal-Diameter Disk-Gap-Band Parachute Deployed at a Mach Number of 1.91 and a Dynamic Pressure of 11.6 Pounds Per Square Foot," Tech. Rep. TM X-1575, Aug 1968.

[8] J. S. Preisser and R. B. Grow, "High Altitude Flight Test of a Reefed 12.2-Meter Diameter Disk-Gap-Band Parachute With Deployment at a Mach Number of 2.58," Tech. Rep. TN D-6469, Aug 1971.

[9] R. D. Moog and F. C. Michel, "Balloon Launched Viking Decelerator Test Program Summary Report," Tech. Rep. CR-112288, 1973.

[10] E. J. Fallon, "System Design Overview of the Mars Pathfinder Parachute Decelerator Subsystem," Tech. Rep. 1997-1511, 1997.

[11] D. A. Spencer, R. Blanchard, R. D. Braun, P. H. Kallemeyn, and S. W. Thurman, "Mars Pathfinder Entry, Descent, and Landing Reconstruction," *Journal of Spacecraft and Rockets*, vol. 36, no. 3, pp. 357–365, May 1999.

[12] J. R. Cruz and J. S. Lingard, "Aerodynamic Decelerators for Planetary Exploration: Past, Present, and Future," Tech. Rep. 2006-6792, 2006.

[13] A. Witkowski and R. Bruno, "Mars Exploration Rover Parachute Decelerator System Program Overview," Tech. Rep. 2003-2100, 2003.

[14] D. S. Adams, A. Witkowski, and M. Kandis, "Phoenix Mars Scout Parachute Flight Behavior and Observations," Tech. Rep. 1534, 2011.

[15] J. R. Cruz, D. W. Way, J. D. Shidner, J. L. Davis, D. S. Adams, and D. S. Kipp, "Reconstruction of the Mars Science Laboratory Performance and Comparison to the Descent Simulation," Tech. Rep. 2013-1250, 2013.

[16] A. Witkowski and R. Bruno, "Mars Pathfinder Parachute System Performance," Tech. Rep. 1999-1701, 1999.

[17] D. S. Adams and N. P. Onufer, "Mars Science Labora- tory Parachute Development Test Program," Tech. Rep. 2011-2508, 2011.

[18] P. T. Zell, J. R. Cruz, and A. Witkowski, "Structural Testing of Parachutes in the National Full-Scale Aerodynamics Complex 80-by-120-Foot Wind Tunnel at NASA Ames Research Center," Tech. Rep. 2003-2130, 2003.

[19] J. C. Gallon, I. G. Clark, and A. Witkowski, "Parachute Decelerator System Performance During the Low Density Supersonic Decelerator Program's First Supersonic Flight Dynamics Test," Tech. Rep. 2015-2130, 2015.

[20] C. O'Farrell, E. J. Brandeau, C. L. Tanner, J. C. Gallon, S. Muppidi, and I. G. Clark, "Reconstructed Parachute System Performance During the Second LDSD Supersonic Flight Dynamics Test," Tech. Rep. 2016-3242, 2016.

[21] J. R. Cruz, D. W. Way, J. D. Shidner, J. L. Davis, R. W. Powell, D. M. Kipp, D. S. Adams, A. Witkowski, and M. Kandis, "Parachute Models Used in the Mars Science Laboratory Entry, Descent, and Landing Simulation," Tech. Rep. 2013-1276, 2013.

[22] W. L. Ludtke, "Wind Tunnel Tests of a 20-Gore Disk-Gap-Ban Parachute," Tech. Rep. 89-180, 1989.

[23] J. R. Cruz, C. O'Farrell, C. H. Zumwalt, and D. F. Keller, "Wind Tunnel Testing of Ringsail and Disk-Gap-Band Parachutes," Tech. Rep. 14-00932, 2015.

[24] R. J. Bendura, E. K. Huckins, and L. C. Coltrane, "Performance of a 19.7-Meter-Diametet Disk-Gap-Band Parachute in a Simulated Martian Environment," Tech. Rep. TM X-1499, Aug 1968.

[25] C. V. Eckstrom and J. S. Preisser, "Flight Test of a 40-Foot-Nominal-Diameter Disk-Gap-Band Parachute Deployed at a Mach Number of 2.72 and a Dynamic Pressure of 9.72 Pounds per Square Foot," Tech. Rep. TM X-1623, Aug 1968.

[26] C. V. Eckstrom, "Flight Test of a 40-Foot-Nominal-Diameter Disk-Gap-Band Parachute Deployed at a Mach Number of 3.31 and a Dynamic Pressure of 10.6 Pounds per Square Foot," Tech. Rep. TM X-1924, Feb 1970.

[27] C. V. Eckstrom and D. R. Branscome, "High-Altitude Flight Test of a Disk-Gap-Band Parachute Deployed Behind a Bluff Body at a Mach Number of 2.69," Tech. Rep. TM X-2671, Dec 1972.

[28] D. Dickinson, F. Hicks, J. Schlemmer, F. Michel, and R. D. Moog, "Balloon Launched Decelerator Test Program Post-Flight Test Report: BLDT Vehicle AV-4," Tech. Rep. CR-112179, 1972.

[29] ——, "Balloon Launched Decelerator Test Program Post-Flight Test Report: BLDT Vehicle AV-2," Tech. Rep. CR-112177, 1972.

[30] ——, "Balloon Launched Decelerator Test Program Post-Flight Test Report: BLDT Vehicle AV-4," Tech. Rep. CR-112179, 1972.

[31] D. E. A. Reichneau, "Aerodynamic Characteristics of Disk-Gap-Band Parachutes in the Wake of Viking Entry Forebodies at Mach Numbers From 0.2 to 2.6," Tech. Rep. AEDC-TR-72-78, 1972.

[32] L. M. Couch, "Drag and Stability Characteristics of a Variety of Reefed and Unreefed Parachute Configurations at Mach 1.80 with an Empirical Correlation for

Supersonic Mach Numbers," Tech. Rep. TR R-429, Aug 1975.

[33] W. C. Alexander and J. T. Faughner, "Drag and Stability Characteristics of High-Speed Parachutes in the Transonic Range," Tech. Rep. 1973-473, 1973.

[34] A. Sengupta, J. Roeder, R. Kelsch, M. Wernet, M. Kandis, and A. Witkowski, "Supersonic Disk Gap Band Parachute Performance in the Wake of a Viking-Type Entry Vehicle from Mach 2 to 2.5," Tech. Rep. 2008-6217, Sep 2008.

[35] G. C. Greene, "Opening Distance of a Parachute," Tech. Rep. 1, 1970.

[36] J. R. Cruz, R. E. Mineck, D. F. Keller, and M. V. Bobskill, "Wind Tunnel Testing of Various Disk-Gap-Band Parachutes," Tech. Rep. 2003-2129, 2003.

[37] C. H. Zumwalt, J. R. Cruz, C. O'Farrell, and D. F. Keller, "Wind Tunnel Test of Subscale Ringsail and Disk-Gap-Band Parachutes," Tech. Rep. 2016-3882, 2016.

[38] J. R. Cruz, C. O'Farrell, E. Hennings, and P. Runnels, "Permeability of Two Parachute Fabrics - Measurements, Modeling, and Application," Tech. Rep. TM 2016-219328, 2016.

[39] I. Nompelis, T. Drayna, and G. V. Candler, "A Parallel Unstructured Implicit Solver for Hypersonic Reacting Flow Simulation," Tech. Rep. 2005-4867, 2003.

[40] C. D. Karlgaard, P. Kutty, M. Schoenenberger, J. Shidner, and M. Munk, "Mars Entry Atmospheric Data System Trajectory Reconstruction Algorithms and Flight Results," Tech. Rep. 2013-0028, 2013.

[41] S. Muppidi, J. W. Van Norman, C. O'Farrell, D. Bose, and I. G. Clark, "Computational Analysis and Post-Flight Validation of Ballute Aerodynamics," Tech. Rep. 2015-2116, March 2015.

[42] T. W. Knacke, "Parachute Recovery Systems Design Manual," Tech. Rep. NWC-TP-6575, 1991.

BIOGRAPHY

Clara O'Farrell is an engineer in the Entry, Descent, and Landing Guidance and Control Systems Group at JPL. She received a PhD in Control and Dynamical Systems from Caltech in 2013, and a BSE in Mechanical and Aerospace Engineering from Princeton University in 2008. Since joining JPL in 2013, she has worked on the Low-Density Supersonic Decelerators and ASPIRE projects.

Suman Muppidi is a Research Scientist at the NASA Ames Research Center. He is currently serving at the Aerosciences lead for the ASPIRE project. He received a B. Tech. from the Indian Institute of Technology, Madras, and a PhD from the University of Minnesota, both in Aerospace Engineering.

Joseph M. Brock is a member of the ASPIRE Aerosciences team. He is a member of the technical staff at NASA Ames Research Center.

John W. Van Norman is a member of the ASPIRE Aerosciences team. He is a member of the technical staff at NASA Langley Research Center.

Ian G. Clark is a Systems Engineer at JPL, and a specialist in the area of Planetary Entry, Descent, and Landing (EDL). Dr. Clark is the recipient of a number of awards including the Presidential Early Career Award for Scientists and Engineers, the JPL Lew Allen Award, and the JPL Explorer Award. He was Principal Investigator of the Low-Density Supersonic Decelerators project. He holds B.S., M.S., and Ph.D. degrees in Aerospace Engineering from the Georgia Institute of Technology, where he also previously served as a Visiting Assistant Professor.